Period-Doubling Optoelectronic Parametric Oscillator for Reconfigurable Microwave Waveform Generation

Liangzun Tang, Shifeng Liu, Changlong Du, Zhenzhou Tang, Simin Li, and Shilong Pan, *Fellow, IEEE*

***Abstract*—In this paper, a novel period-doubling optoelectronic parametric oscillator (OEPO) based on the in-loop nonlinear dynamics is proposed. The proposed system is built upon the conventional single-loop optoelectronic oscillator (OEO) architecture, incorporating an additional broadband filter in parallel with the narrowband filter. By injecting an external microwave signal into the OEO, two mutually coupled oscillation modes, whose sum frequency equals the injected microwave signal, can simultaneously survive and oscillate. The two oscillating frequencies reach self-consistency every two round trips through frequency conversion and energy coupling in the Mach-Zehnder modulator (MZM) and the photodetector. When the loop gain slightly exceeds the oscillation threshold, the OEPO can oscillate at two pure frequencies with proper phase matching. As the loop gain gradually increases to a sufficiently high level, a Hopf bifurcation will occur in the amplitudes of the two surviving modes due to nonlinear effects, leading to frequency-hopping behavior in the output microwave waveform. In a proof-of-concept experiment, the OEPO successfully generates a phase-coherent dual-frequency microwave signal or a frequency-hopping microwave signal with frequencies ranging from 6.5 to 12 GHz. This work demonstrates a novel oscillation mechanism in OEPO, providing reconfigurable microwave waveform generation capabilities that could be applied in emerging wireless communications and advanced electronic warfare systems.**

***Index Terms*—Microwave generation, microwave photonics, optoelectronic parametric oscillator.**

I. Introduction

OPTOELECTRONIC oscillators (OEOs) are nonlinear, dissipative, time-delayed, and spontaneous microwave photonic systems that have been extensively studied for various applications. A key advantage of OEOs is their capability to generate high-frequency signals (tens of GHz) with ultralow phase noise, which is crucial for applications such as wireless communication [1], radar [2], electronic warfare [3], [4], [5], and metrology. Traditionally, commercial high-frequency microwave signals are generated by multiplying the output frequency of a conventional low-frequency (tens of MHz) oscillator, such as a voltage-controlled oscillator [6] or a quartz crystal oscillator [7]. However, this method often results in significant phase noise deterioration due to the frequency multiplication process. In contrast, OEOs use narrowband electrical filters [8], [9], [10], [11], [12], [13], [14], optical filters [15], [16], [17], [18], [19], [20], [21], or equivalent microwave photonic filters [22], [23], [24], [25] for effective mode selection and can generate high-frequency single-mode microwave signals. Moreover, OEOs have been demonstrated as a viable method for radio-frequency (RF) synthesized signal generation [26], [27], offering optimized phase noise performance for various signals including dual-frequency RF [28], [29], frequency-hopping microwave signals [30], [31], [32], linearly frequency-chirped signals [33], [34], [35], [36], [37], [38], [39], and arbitrary microwave waveforms [40], [41], [42]. When the loop gain is sufficiently high, nonlinear effects within OEOs, due to the inherent nonlinearity of intracavity electrical-optical modulators or RF amplifiers, significantly affect the amplitudes of the oscillating signals. These nonlinearities, combined with loop delay, lead to complex dynamical behaviors such as solitons [43], [44], [45], chaos [46], [47], [48], [49], and bifurcations [50], [51], [52], [53], [54]. Recently, an optoelectronic parametric oscillator (OEPO) [55] was proposed, capable of achieving parametric frequency down-conversion in the optoelectronic domain through intracavity nonlinearity. Similar to an optical parametric oscillator (OPO), an OEPO can be regarded as a coherent microwave source with a wide range of applications, including communication, navigation, and radar systems. However, the coherent microwave signal generated by the OEPO in [55] is symmetrically distributed over a narrow bandwidth, limiting its practical applications.

In this paper, we propose a broadband OEPO with period-doubling oscillation based on intracavity nonlinear dynamics. The proposed system features a broadband filter connected in parallel with a narrowband filter, creating two oscillation loops with equal round-trip times. This parallel filter arrangement enables the oscillation of two nondegenerate modes and facilitates the parametric oscillation procedure introduced by the intracavity nonlinear mechanism.

Received 14 August 2024; revised 8 December 2024; accepted 11 December 2024. Date of publication 13 December 2024; date of current version 2 April 2025. This work was supported in part by the National Key R&D Program of China under Grant 2022YFB2802704, in part by the Jiangsu Funding Program for Excellent Postdoctoral Talent under Grant 2022ZB237, and in part by the National Natural Science Foundation of China under Grant 62271249 and Grant 62071226. *(Corresponding author: Shifeng Liu.)*

The authors are with the National Key Laboratory of Microwave Photonics, Nanjing University of Aeronautics and Astronautics, Nanjing 210016, China (e-mail: lztang@nuaa.edu.cn; sfliu_nuaa@nuaa.edu.cn; 820562146dcl@nuaa.edu.cn; tangzhzh@nuaa.edu.cn; lisimin@nuaa.edu.cn; pans@ieee.org).

Color versions of one or more figures in this article are available at https://doi.org/10.1109/JLT.2024.3517877.

Digital Object Identifier 10.1109/JLT.2024.3517877

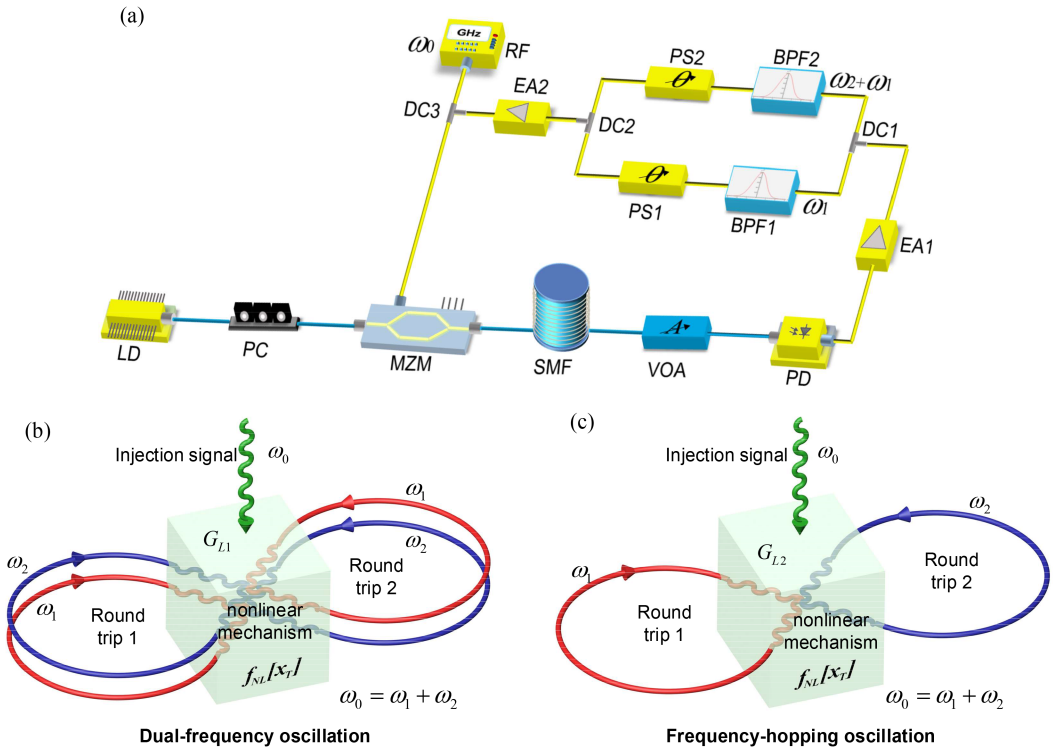

Fig. 1. (a) Schematic diagram of the proposed period-doubling OEPO; (b) the dual-frequency oscillation state when the loop gain of the OEPO is G_{L1}; (c) the frequency-hopping oscillation state when the loop gain of the OEPO is G_{L2}. LD: laser diode; PC: polarization controller; MZM: Mach-Zehnder modulator; SMF: single-mode fiber; VOA: variable optical attenuator; PD: photodetector; EA: electrical amplifier; DC: directional coupler; BPF; band-pass filter; PS: phase shifter; RF: radio frequency.

The Mach-Zehnder modulator (MZM) in the OEPO acts as the nonlinear medium for parametric oscillation and operates at the minimum transmission bias (MITB) point to achieve carrier-suppressed double sideband (CS-DSB) modulation. An external RF signal is injected to the proposed OEPO via the MZM to stimulate the nonlinear frequency conversion and energy coupling between different oscillation modes. The frequency of the injection signal is the sum of the two oscillation modes. The mixed frequency component of the injection signal and one oscillation mode contributes to the stable oscillation of the other mode, provided there is proper phase matching and sufficient loop gain. Under these conditions, two mutually coupled oscillation modes can simultaneously survive and oscillate in the OEPO. By adjusting the loop gain, two distinct oscillation states—dual-frequency and frequency-hopping—can be achieved, which were previously unexplored. Additionally, frequency tunability of the oscillation mode is facilitated by the wideband filter and the time-delayed parametric oscillation process.

II. Principle of Operation and Simulation Results

Fig. 1(a) illustrates the schematic diagram of the proposed OEPO system. The system, characterized by a closed feedback loop, consists of two coupled branches: an optical branch and an electronic branch. In the optical branch, an optical signal from a continuous-wave (CW) laser is modulated by feedback signals in the MZM and then converted into electrical signals by the photodetector (PD). In the electronic branch, the electrical signals from the PD are amplified, filtered, and phase-shifted before being fed back to the MZM along with the external RF signal. Unlike conventional single-loop OEOs, an additional broadband filter in parallel with the narrowband filter is used to achieve a broadband operating frequency. Fig. 1(b) and (c) show the frequency conversion and energy coupling between the two oscillation modes through the nonlinear medium in the proposed period-doubling OEPO. In Fig. 1(b), the OEPO operates in a dual-frequency oscillation state when the loop gain G_{L1} slightly exceeds the oscillation threshold. In this state, two nondegenerate modes oscillate simultaneously and convert into each other during the next round trip. As the loop gain increases to a sufficiently high level, the OEPO transitions to the frequency-hopping state shown in Fig. 1(c). In this state, only one nondegenerate mode oscillates during each round trip due to the intracavity nonlinear mechanism and the gain competition. The nonlinearity primarily originates from the MZM, which is biased at the MITB point. Through the electro-optical conversion and opto-electrical conversion in the MZM and PD, the energy coupling and frequency conversion are achieved between the two oscillation modes. Since the oscillation frequencies require two round trips to achieve self-consistency, the OEPO operates under a period-doubling state.

Generally, we assume that the angular frequencies of the injected signal and the oscillating signal are ω_0 and ω_{osc} ($\omega_0 >$

ω_{osc}), respectively. Ignoring the high-order sidebands generated by the MZM biased at the MITB point, the frequencies of the output signal from the PD are $2\omega_0$, $2\omega_{osc}$, $\omega_0+\omega_{osc}$, ω_0-ω_{osc}. A broadband filter is employed to remove the sum-frequency and other harmonic components. To sustain oscillation, the remaining frequency components must match the oscillating signal, i.e., ω_0-$\omega_{osc}=\omega_{osc}$. In this case, the OEPO operates in a degenerate oscillation state and functions as a 1/2-scaled microwave frequency divider, as detailed in [56].

A. Dual-Frequency Signal

Here we discuss the case of nondegenerate oscillation. Assume the oscillating signal in the closed feedback loop is $V_{osc}=A_1\cos(\omega_1 t+\theta_1)+A_2\cos(\omega_2 t+\theta_2)$, and the injected signal is $V_{in}=A_0\cos(\omega_0 t+\theta_0)$, where A_0, A_1, A_2, ω_0, ω_1, ω_2, θ_0, θ_1, and θ_2 are the amplitudes, angular frequencies and phases of the injected signal and the two nondegenerate oscillation frequency components, respectively. The output optical signal of the MZM could be written as

$$\begin{aligned}E_{out}(t)=E_{in}/2\cdot[&\exp(j\omega_c t-j\beta_0\cos(\omega_0 t+\theta_0)\\&-j\beta_1\cos(\omega_1 t+\theta_1)-j\beta_2\cos(\omega_2 t+\theta_2))\\&+\exp(j\omega_c t+j\beta_0\cos(\omega_0 t+\theta_0)+j\beta_1\cos(\omega_1 t\\&+\theta_1)+j\beta_2\cos(\omega_2 t+\theta_2)+j\varphi)]\end{aligned}\tag{1}$$

where E_{in} and ω_c are the amplitude and angular frequency of the optical carrier, $\beta_0=\pi A_0/V_\pi$, $\beta_1=\pi A_1/V_\pi$, $\beta_2=\pi A_2/V_\pi$ are the modulation index of the externally injected signal and oscillating signal, φ is the phase difference between the two arms of the MZM. To achieve CS-DSB modulation, the phase difference φ is set to π.

After traveling through a length of single-mode fiber, the optical signal is converted into an electrical signal by a PD. The resulting output current can be expressed as

$$\begin{aligned}i_{PD}=\frac{a_L\Re E_{in}^2}{2}[&1-\cos(\beta_0\cos(\omega_0(t-T)+\theta_0)\\&+\beta_1\cos(\omega_1(t-T)+\theta_1)+\beta_2\cos(\omega_2(t-T)+\theta_2))]\end{aligned}\tag{2}$$

where $\Re$ is the responsivity of the PD, a_L and T are the transmission coefficient and the time delay of the oscillation loop. According to the Jacobi-Anger expansion and neglecting high-order harmonics and high-frequency mixing signals, the output RF signal could be rewritten as

$$\begin{aligned}i_{PD}=a_L\Re E_{in}^2[&J_0(\beta_0)J_1(\beta_1)J_1(\beta_2)\\&\times\cos((\omega_2-\omega_1)(t-T)+\theta_2-\theta_1)\\&+J_0(\beta_1)J_1(\beta_0)J_1(\beta_2)\cos((\omega_0-\omega_2)(t-T)\\&+\theta_0-\theta_2)+J_0(\beta_2)J_1(\beta_0)J_1(\beta_1)\\&\times\cos((\omega_0-\omega_1)(t-T)+\theta_0-\theta_1)]\end{aligned}\tag{3}$$

where J_n is the n-th order Bessel function of the first kind. For sustained and stable oscillation in the OEPO, the output RF signal, after filtering, phase shifting and amplifying should match the input oscillating signal in the MZM. The low-frequency component ω_2-ω_1 is filtered out by the band-pass filter. Therefore, we obtain

$$\begin{cases}\omega_0=\omega_1+\omega_2\\ \theta_1=\theta_0-\theta_2-(\omega_0-\omega_2)T+\phi_1+2k_1\pi\\ \theta_2=\theta_0-\theta_1-(\omega_0-\omega_1)T+\phi_2+2k_2\pi\\ A_1=a_L\Re E_{in}^2R_{PD}G_1J_0(\beta_1)J_1(\beta_0)J_1(\beta_2)\\ A_2=a_L\Re E_{in}^2R_{PD}G_2J_0(\beta_2)J_1(\beta_0)J_1(\beta_1)\end{cases}\tag{4}$$

where ϕ_1, ϕ_2 and G_1, G_2 are the phase shifts introduced by the phase shifters and the total gain coefficients of the electronic branches for the frequency components ω_0-ω_2 and ω_0-ω_1, $R_{\rm PD}$ is the matched load of the PD, and k_1 and k_2 are the different integers corresponding to the mode orders. According to (4), two different frequency components whose sum frequency equals the injected frequency can oscillate simultaneously under appropriate loop gain and phase conditions. However, if the frequency response of the electrical path is completely flat, the mode pair of the nondegenerate oscillation is random. To obtain a desired oscillating signal, a narrowband filter (tens of MHz) is used in parallel connection with the broadband filter so that the frequency response of the whole electronic branch is equivalent to a flat shape with a slight peak. This configuration causes the OEPO to preferentially oscillate at the frequency of the peak. Consequently, the oscillating mode pair for the nondegenerate oscillation becomes fixed. This setup allows for the generation of a dual-frequency microwave signal, with one frequency fixed at the center of the narrowband filter and the other varying with the injected signal. It is worth mentioning that the two generated frequency components are phase coherent and have a better phase noise performance compared to the injected signal near 10-kHz offset.

B. Frequency-Hopping Signal

When the loop gain gradually increases to a sufficiently high level, a supercritical Hopf bifurcation will occur due to the nonlinear dynamics of the OEPO. Similar nonlinear bifurcation behaviors have been analyzed in broadband/narrowband OEOs [57], [58], [59] and SBS-based tunable OEO [60]. Reference [59] proposes a time-domain approach using delay-differential equations (DDEs) to study the nonlinear dynamics of narrowband OEOs. For the case of external RF injection in our configuration, the DDEs can be expressed as

$$\begin{cases}V_1(t)+\frac{1}{\Delta\omega_1}\frac{dV_1(t)}{dt}+\frac{\omega_1^2}{\Delta\omega_1}\int_{t_0}^{t}V_1(s)ds\\ =a_LG_1SP_0f_{NL}[V_2(t-T)+V_{in}(t-T)]\\ V_2(t)+\frac{1}{\Delta\omega_1}\frac{dV_2(t)}{dt}+\frac{\omega_2^2}{\Delta\omega_1}\int_{t_0}^{t}V_2(s)ds\\ =a_LG_2SP_0f_{NL}[V_1(t-T)+V_{in}(t-T)]\end{cases}\tag{5}$$

where ω_1 and ω_2 are the angular center frequencies of the oscillating signals, $\Delta\omega_1$ is the bandwidth of the narrowband filter, P_0 is the output power of the CW laser, and $S=\Re R_{\rm PD}$ is the conversion factor of the PD. In these equations, $V_{osc}(t)=V_1(t)+V_2(t)$ represents the oscillating microwave signal, while $f_{NL}[x_T]=\cos^2(\pi x_T/2V_\pi+\varphi/2)$ denotes the nonlinearity from the MZM, where V_π and φ are the half-wave voltage and offset phase of the MZM. Since the two oscillation modes are mutually

coupled and limited by the narrowband response of the filter, the microwave signal can be written as $V_{osc}(t) = V_1(t) + V_2(t) = A_1(t)\cos(\omega_1 t + \theta_1) + A_2(t)\cos(\omega_2 t + \theta_2)$, where $A_1(t)$ and $A_2(t)$ are the slowly varying complex amplitudes on the timescale of approximately $1/\Delta\omega_1$. Given that the MZM is bias at the MITB point ($\varphi = \pi$) and applying the Jacobi-Anger expansion, (5) could be expressed as

$$\begin{cases} V_1(t) + \frac{1}{\Delta\omega_1}\frac{dV_1(t)}{dt} + \frac{\omega_1^2}{\Delta\omega_1}\int_{t_0}^{t} V_1(s)ds \\ = a_L S G_1 P_0 J_1\left[\frac{\pi A_{\text{in}}}{V_\pi}\right] J_1\left[\left|\frac{\pi A_2(t-T)}{V_\pi}\right|\right] \\ \cos(\omega_1(t-T) + (\theta_0 - \theta_2)) \\ V_2(t) + \frac{1}{\Delta\omega_1}\frac{dV_2(t)}{dt} + \frac{\omega_2^2}{\Delta\omega_1}\int_{t_0}^{t} V_2(s)ds \\ = a_L S G_2 P_0 J_1\left[\frac{\pi A_{\text{in}}}{V_\pi}\right] J_1\left[\left|\frac{\pi A_1(t-T)}{V_\pi}\right|\right] \\ \cos(\omega_2(t-T) + (\theta_0 - \theta_1)) \end{cases} \tag{6}$$

To simplify the integral terms in (6), we introduce the intermediate variables μ_1 and μ_2

$$\begin{cases} \mu_1(t) = \int_{t_0}^{t} V_1(s)ds \\ \mu_2(t) = \int_{t_0}^{t} V_2(s)ds \end{cases} \tag{7}$$

which are nearly sinusoidal near zero. Therefore, they can be expressed as

$$\begin{cases} \mu_1(t) = \frac{1}{2}\mathcal{B}_1(t)e^{j\omega_1 t} + \frac{1}{2}\mathcal{B}_1^*(t)e^{j\omega_1 t} \\ \mu_2(t) = \frac{1}{2}\mathcal{B}_2(t)e^{j\omega_2 t} + \frac{1}{2}\mathcal{B}_2^*(t)e^{j\omega_2 t} \end{cases} \tag{8}$$

where $\mathcal{B}_1(t)$ and $\mathcal{B}_2(t)$ are the complex amplitudes of the intermediate variables. By substituting (8) into (6) and cancelling the common phase terms $e^{j\omega_1 t}$ and $e^{j\omega_2 t}$, we can obtain

$$\begin{cases} \ddot{\mathcal{B}}_1 + (\Delta\omega_1 + 2j\omega_1)\dot{\mathcal{B}}_1 + j\omega_1\Delta\omega_1\mathcal{B}_1 \\ = 2\Delta\omega_1 a_L S G_1 P_0 J_1\left[\frac{\pi A_{\text{in}}}{V_\pi}\right] \\ \quad \times J_1\left[\left|\frac{\pi(\dot{\mathcal{B}}_2(t-T) + j\omega\mathcal{B}_2(t-T))}{V_\pi}\right|\right] e^{j\varphi_1} \\ \ddot{\mathcal{B}}_2 + (\Delta\omega_1 + 2j\omega_2)\dot{\mathcal{B}}_2 + j\omega_2\Delta\omega_1\mathcal{B}_2 \\ = 2\Delta\omega_1 a_L S G_2 P_0 J_1\left[\frac{\pi A_{\text{in}}}{V_\pi}\right] \\ \quad \times J_1\left[\left|\frac{\pi(\dot{\mathcal{B}}_1(t-T) + j\omega\mathcal{B}_1(t-T))}{V_\pi}\right|\right] e^{j\varphi_2} \end{cases} \tag{9}$$

where $\varphi_1 = \theta_0\text{-}\theta_2\text{-}\omega_1 T$, $\varphi_2 = \theta_0\text{-}\theta_1\text{-}\omega_2 T$. Considering the slowly varying conditions

$$\begin{cases} \left|\ddot{\mathcal{B}}_1\right| \ll \omega_1 \left|\dot{\mathcal{B}}_1\right| \ll \omega_1^2 |\mathcal{B}_1| \\ \left|\ddot{\mathcal{B}}_2\right| \ll \omega_2 \left|\dot{\mathcal{B}}_2\right| \ll \omega_2^2 |\mathcal{B}_2| \end{cases} \tag{10}$$

Eq. (9) can be reduced to

$$\begin{cases} 2j\omega_1\dot{\mathcal{B}}_1 + j\omega_1\Delta\omega_1\mathcal{B}_1 \\ = 2\Delta\omega_1 a_L S G_1 P_0 J_1\left[\frac{\pi A_{\text{in}}}{V_\pi}\right] J_1\left[\left|\frac{j\pi\omega\mathcal{B}_2(t-T)}{V_\pi}\right|\right] e^{j\varphi_1} \\ 2j\omega_2\dot{\mathcal{B}}_2 + j\omega_2\Delta\omega_1\mathcal{B}_2 \\ = 2\Delta\omega_1 a_L S G_1 P_0 J_1\left[\frac{\pi A_{\text{in}}}{V_\pi}\right] J_1\left[\left|\frac{j\pi\omega\mathcal{B}_1(t-T)}{V_\pi}\right|\right] e^{j\varphi_2} \end{cases} \tag{11}$$

From (7) and (8), we obtain $A_1(t) = j\omega_1$ and $\mathcal{B}_1(t) = j\omega_2$ and $\mathcal{B}_2(t)$. Therefore, the complex envelopes $A_1(t)$ and $A_2(t)$ of the microwave signals $V_1(t)$, $V_2(t)$ could be written as follows:

$$\begin{cases} \frac{dA_1(t)}{dt} = -\frac{\Delta\omega_1}{2}A_1(t) + \frac{\Delta\omega_1 G_{L1} V_\pi}{\pi} J_1\left[\frac{\pi|A_2(t-T)|}{V_\pi}\right] e^{j\varphi_1} \\ \frac{dA_2(t)}{dt} = -\frac{\Delta\omega_1}{2}A_2(t) + \frac{\Delta\omega_1 G_{L2} V_\pi}{\pi} J_1\left[\frac{\pi|A_1(t-T)|}{V_\pi}\right] e^{j\varphi_2} \end{cases} \tag{12}$$

where $G_{L1} = \pi a_L S G_1 P_0 J_1[\pi A_{\text{in}}/V_\pi]/V_\pi$, $G_{L2} = \pi a_L S G_2 P_0 J_1[\pi A_{\text{in}}/V_\pi]/V_\pi$ are the loop gain for frequency components ω_1 and ω_2, respectively. By performing a stability analysis of the coupled equations, we can deduce that the variation period of the complex envelope $T_{\text{H}} \approx 2T = 2n_{\text{eff}}L/c$, where n_{eff} and L are the effective refractive index and length of the optical fiber, respectively, and c is the speed of light in a vacuum.

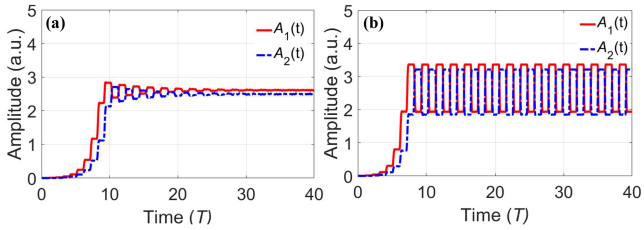

Fig. 2. Numerical simulations of the complex amplitudes developing with time. (a) Converging to a fixed value. (b) Periodic oscillation.

C. Simulations

Since the (12) consists of coupled delay differential equations, deriving analytical solutions is challenging. Therefore, we employ the fourth-order Runge-Kutta method to numerically simulate the evolution of the envelopes. Fig. 2 displays the numerical simulations of the complex amplitudes over time. In Fig. 2(a) and (b), the simulation parameters based on the experimental setup are as follows: (a) $\Delta\omega_1 = 12.5$ MHz, $V_\pi = 3.5$ V, $G_{L1} = G_{L2} = 2.2$, $\varphi_1 = 0.3$, $\varphi_2 = 0.4$; (b) $\Delta\omega_1 = 12.5$ MHz, $V_\pi = 3.5$ V, $G_{L1} = G_{L2} = 2.6$, $\varphi_1 = 0.3$, $\varphi_2 = 0.4$. The initial condition is $[A_1(t), A_2(t)] = [1 \times 10^{-2}, 1 \times 10^{-2}]$ over the interval $[-T, 0]$. In Fig. 2(a), the complex amplitudes converge to fixed values, representing a dual-frequency microwave solution of the DDEs. In Fig. 2(b), the complex amplitudes exhibit square-wave modulated with a period approximately equal to $2T$ when oscillation is stable. The energy of the two frequency components is complementary, leading to a transfer of energy between components every period T, resulting in a frequency-hopping phenomenon in the output microwave waveform.

The numerical simulations of the complex amplitudes as functions of loop gain and external injection power are shown in Fig. 3. In Fig. 3(a) and (b), the simulation parameters based on the experimental setup are as follows: (a) $\Delta\omega_1 = 12.5$ MHz, $A_{\text{in}} = 20$ dBm, $\varphi_1 = 0.3$, $\varphi_2 = 0.4$; (b) $\Delta\omega_1 = 12.5$ MHz, $V_\pi = 3.5$ V, $\Re = 0.65$ A/W, $R_{\text{PD}} = 50\ \Omega$, $P_0 = 17.5$ dBm, $a_L = 4 \times 10^{-5}$, $G_1 = G_2 = 46$ dB, $\varphi_1 = 0.3$, $\varphi_2 = 0.4$. Fig. 3(a) indicates that the amplitudes of the oscillating signals are governed by the total loop gain. For $G_{L1}\&G_{L2} < 1$, the amplitudes are zero, and the OEPO does not oscillate. For $1 \leq G_{L1}\&G_{L2} < 2.3$, the amplitudes converge to fixed non-zero points and the

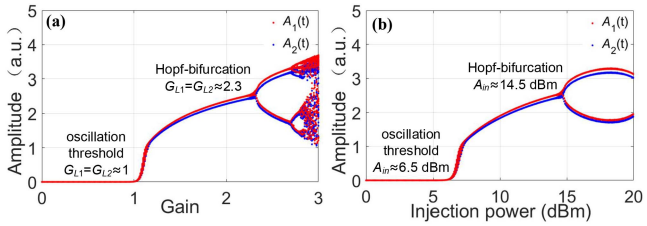

Fig. 3. Numerical simulations of the complex amplitudes varying with: (a) loop gain; (b) external injection power.

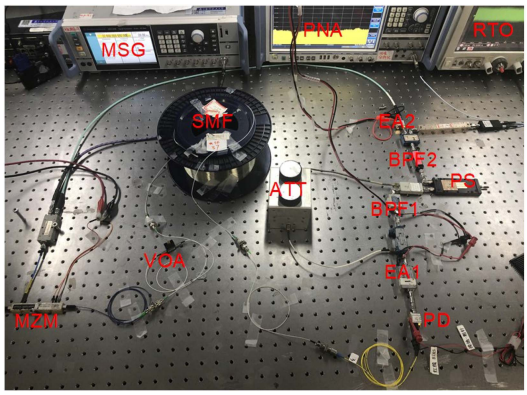

Fig. 4. The illustration of the experimental setup. ATT: attenuator; MSG: microwave signal generator; PNA: phase noise analyzer; RTO: real-time oscilloscope.

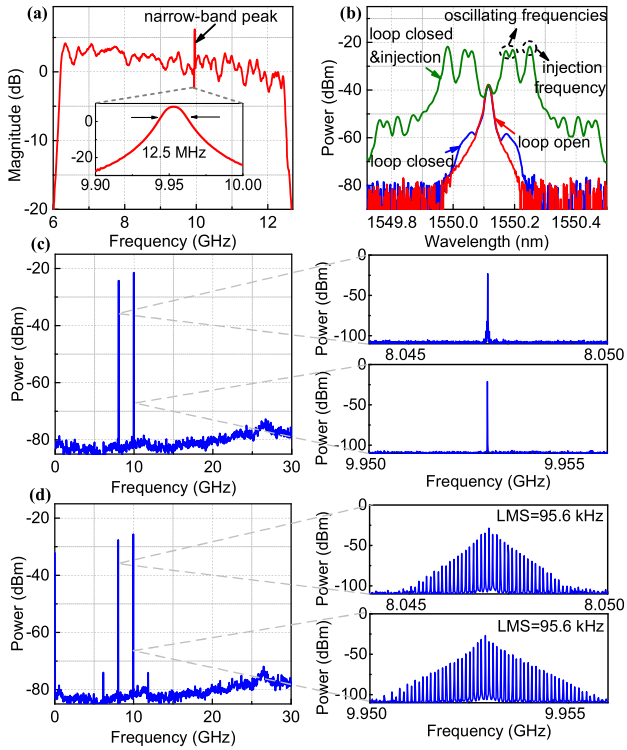

Fig. 5. (a) The open-loop magnitude response of the OEPO and corresponding zoomed-in view of the narrow-band peak. (b) The measured spectra of the input optical signal before the PD. The frequency spectra (RBW = 100 kHz) and corresponding zoomed-in view (RBW = 100 Hz) of the generated (c) dual-frequency signal and (d) frequency-hopping signal.

OEPO outputs dual-frequency microwave signal. For $2.3 \leq G_{L1}\&G_{L2} < 2.7$, the amplitudes undergo Hopf bifurcation to periodic oscillations and the OEPO outputs frequency-hopping microwave signal. For $G_{L1}\&G_{L2} \geq 2.7$, the amplitudes bifurcate further, evolving into a chaotic state. This study focuses on the range $1 \leq G_{L1}\&G_{L2} < 2.7$. We also investigated the relationship between the amplitudes and the injection power. As depicted in Fig. 3(b), the injection powers corresponding to the oscillation thresholds and the Hopf-bifurcation points are about 6.5 dBm and 14.5 dBm, respectively. When the amplitudes reach their maximum values, the corresponding injection power is about 16.2 dBm.

III. Experimental Results

To investigate the performance of the proposed system, an experiment based on the setup in Fig. 1(a) is carried out. The experimental setup is illustrated in Fig. 4. In the experiment, an optical carrier centered at 1550.12 nm with a power of 17.5 dBm is produced by a CW laser (Teraxion PS-NLL). The optical carrier is then sent to an MZM (Fujitsu FTM 7938EZ) with a half-wave voltage of 3.5 V. After passing through a 1.05-km single-mode fiber, the output optical signal is converted to electrical signal by a PD (u2t XPDV2120RA) with a responsivity of 0.65 A/W. A variable optical attenuator (VOA) is used before the photodetector to adjust the input optical power. Two power amplifiers are employed to amplify the generated electrical signal. The first amplifier (EA1) offers a gain of 20 dB and a saturated output power of 17 dBm, while the second amplifier (EA2) provides a gain of 26 dB and a saturated output power of 23 dBm. Two parallel microwave band-pass filters are employed for mode selection: a narrowband filter (BPF1) with a center frequency of 9.953 GHz and a 3-dB bandwidth of 12.5 MHz, and a broadband filter (BPF2) with a passband of 6.3–12.4 GHz. A phase shifter (PS) with a bandwidth of 6–18 GHz is used to adjust the loop delay. After passing through these two branches, the electrical signal, along with an external RF signal generated by a microwave signal generator (R&S SMA100B), is fed back to the MZM.

In the first step, the loop gain is adjusted to be slightly below the free-oscillation threshold by tuning the VOA. An external microwave signal with a frequency of 18 GHz and a power of 15 dBm is then injected into the OEPO system, bringing the effective loop gain to the free-oscillation threshold. As a result, the OEPO begins oscillating at frequencies of 9.953 GHz and 8.047 GHz, producing a dual-frequency microwave signal. In this state, the optical power before PD and the electrical power after EA2 are −3.5 dBm and 14.8 dBm, respectively. Further increasing the loop gain to the Hopf-bifurcation point by reducing the insertion loss of the VOA causes the OEPO to enter a nonlinear dynamic state, resulting in a frequency hopping microwave signal. In this state, the optical power before PD and the electrical power after EA2 are 0.2 dBm and 16.5 dBm, respectively. Fig. 5(a) illustrates the open-loop magnitude response of the OEPO, measured by a vector network

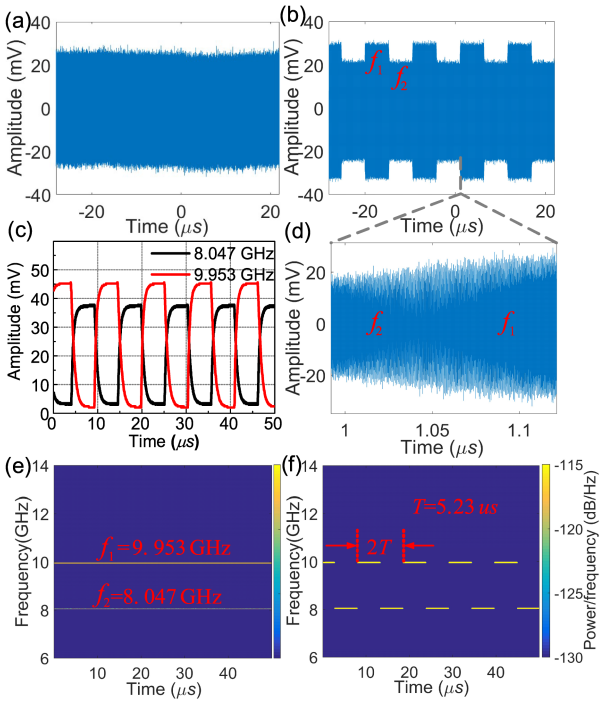

Fig. 6. Temporal waveform of the output (a) dual-frequency microwave signal and (b) frequency-hopping microwave signal. (c) The amplitude envelopes of the two frequency components in frequency-hopping microwave signal. (d) The zoomed-in view of temporal waveform at the frequency-hopping point. The instantaneous frequency-time diagrams for (e) dual-frequency microwave signal and (f) frequency-hopping microwave signal.

analyzer (R&S ZVA-67), showing a passband of approximately 6.3–12.4 GHz. Additionally, the narrowband peak centered at 9.953 GHz has a bandwidth of about 12.5 MHz. Fig. 5(b) presents the spectra of the input optical signal before the photodetector under different conditions, measured by an optical spectrum analyzer (YOKOGAWA AQ6370). As can be seen, the MZM is biased at the carrier suppression point, resulting in no output from the OEPO without external microwave signal injection. With the external signal injection, the oscillation will start up and two new $\pm$1st order sidebands appear between the optical carrier and the injection signal, which correspond to the oscillating signal. Fig. 5(c) and (d) show the electrical spectra and their corresponding zoomed-in views of the oscillating signals, measured by a phase noise analyzer (R&S FSWP50) under varying loop gains. Observations show that the longitudinal mode spacing (LMS) of the OEPO is 95.6 kHz, approximately half of the cavity free spectral range (FSR) for the 1.07-km single-mode fiber. This suggests that the OEPO operates under a period-doubling mechanism. Fig. 5(c) shows that when the total loop gain slightly exceeds the oscillation threshold, the OEPO oscillates at two distinct monochromatic frequencies. In Fig. 5(d), when the loop gain significantly surpasses the oscillation threshold and exceeds the Hopf-bifurcation point, a stable mode-locked frequency-hopping signal is generated.

Temporal waveforms of the output signals, measured with a real-time oscilloscope (Keysight DSOX93304, 80 GSa/s), are shown in Fig. 6(a) and (b). Fig. 6(b) shows a stable

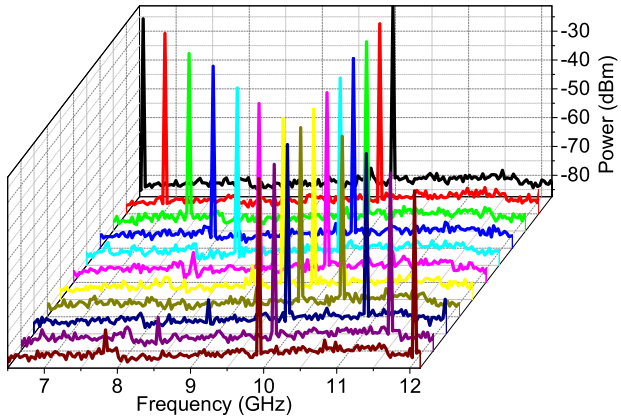

Fig. 7. Electrical spectra (RBW = 100 kHz) of the output dual-frequency signals with one frequency component fixed at 9.953 GHz and the other varying from 6.5 GHz to 12 GHz with a step of 0.5 GHz.

frequency-hopping pulse sequence with a pulse period of 10.46 µs, approximately twice the round-trip time of the OEPO. The amplitude envelopes of the two frequency components, measured by a digital oscilloscope (RIGOL MSO2302A, 2GSa/s), are shown in Fig. 6(c). These results align with the simulation shown in Fig. 2(b). Fig. 6(d) provides a zoomed-in view of the temporal waveform during frequency hopping, demonstrating a rapid frequency-switching speed of up to tens of nanoseconds. Fig. 6(e) and (f) shows the instantaneous time-frequency diagrams for both the dual-frequency microwave signal and the frequency-hopping microwave signal. The two carrier frequencies are centered at 8.047 GHz and 9.953 GHz.

A. *Frequency Tunability*

To investigate the frequency tunability of the proposed system, external microwave signals with frequencies ranging from 16.5 GHz to 22 GHz are applied to the OEPO. The experimental setup and device parameters remain as described above. First, the total loop gain is adjusted to slightly exceed the free-oscillation threshold. By tuning the phase shifters, the phase matching condition is achieved. Subsequently, the OEPO begins oscillating and outputs dual-frequency microwave signal. The electrical spectra of these dual-frequency signals are shown in Fig. 7. One frequency component of the dual-frequency signal remains fixed at the center of the narrowband filter, while the other varies within the passband of the broadband filter. The sum of the two frequency components equals the frequency of the injected signal, demonstrating microwave parametric down-conversion.

The total loop gain is then adjusted to exceed the Hopf-bifurcation point, enabling the OEPO to produce frequency-hopping microwave signals. By varying the frequency of the injection signal from 16.5 GHz to 21.5 GHz with a step of 1 GHz, the instantaneous frequency-time diagrams of the output frequency-hopping signals are depicted in Fig. 8. Notably, the fixed frequency component can also be adjusted using a tunable narrowband electrical filter, such as an yttrium iron garnet (YIG) filter. The frequency tuning range of the output signal is primarily constrained by the bandwidth of the broadband electrical filter.

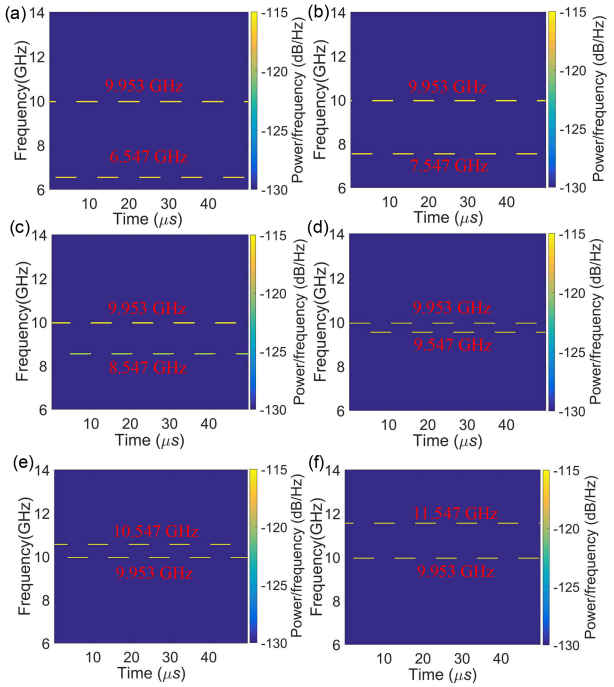

Fig. 8. Instantaneous frequency-time diagrams of the frequency-hopping microwave signals with one carrier frequency fixed at 9.953 GHz and the other changing from 6.547 GHz to 11.547 GHz with a step of 1 GHz.

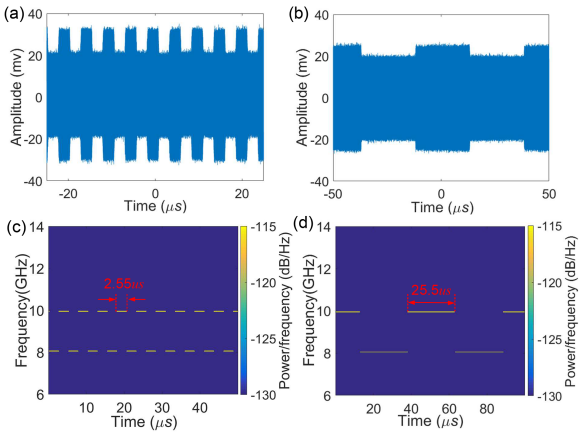

Fig. 9. Temporal waveforms and instantaneous frequency-time diagrams of frequency-hopping signals with different fiber lengths: (a) and (c) for 500 m, (b) and (d) for 5 km.

Since the period of the frequency-hopping signal is related to the OEPO's cavity delay, it can be adjusted by changing the length of the single-mode fiber. Fig. 9 shows the temporal waveforms and corresponding frequency-time diagrams for the frequency-hopping signals generated by the OEPO with fiber lengths of 500 m and 5 km.

B. Phase Noise Performances and Phase Coherent

The phase noise performances of the generated signals and commercial electrical sources, measured by a phase noise analyzer, are shown in Fig. 10. The generated signals were obtained using a 1.05-km fiber and an 18-GHz external injection

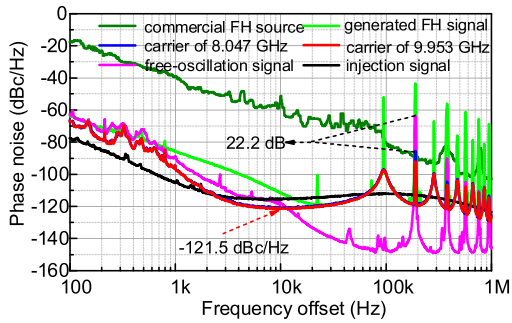

Fig. 10. Comparison of the phase noise performance of the generated signals and commercial electrical sources.

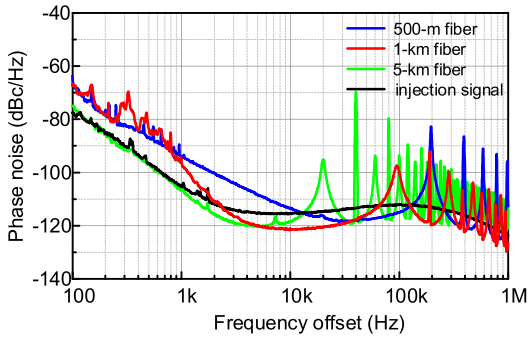

Fig. 11. Comparison of the phase noise performance of the output dual-frequency signals with different single-mode fiber lengths.

signal in the OEPO setup. The phase-noise curves of the two frequency components (red and blue line) of the generated dual-frequency signal are approximately the same and as low as −121.5 dBc/Hz at 10-kHz frequency offset. Compared to the injected signal (black line), the dual-frequency signal has a better performance around 10-kHz frequency offset. Additionally, the side-mode suppression ratio is approximately 90 dB, representing over a 22-dB improvement compared to the free-running OEO (pink line). The experimental setup of the free-running OEO is generally similar to that of the OEPO, with the main difference being that the OEO uses only a single electrical branch containing BPF1 and does not incorporate external injection. The phase noise of the frequency-hopping signal (green line) is about −112.7 dBc/Hz @ 10 kHz, significantly better than the commercial frequency-hopping signal (olive line) from an arbitrary waveform generator (Keysight M8195A). At low frequency offsets (<10 kHz), the phase noise of the frequency-hopping signal has a more than 40-dB improvement compared to the commercial source, indicating superior short-term stability of the OEPO-generated signals.

To examine the effect of fiber length on the phase noise performance of the output dual-frequency signal, single-mode fibers of 500 m (blue line), 1 km (red line), and 5 km (green line) are used in the OEPO. The corresponding phase noise curves are shown in Fig. 11. There is no significant improvement in phase noise performance as the fiber length increases. This is primarily because the ±1st order sidebands generated by the

TABLE I
COMPARISON OF THE MICROWAVE SIGNAL GENERATION BASED ON OEOS

Scheme	Output signal	Innovation	Frequency tunability	Typical phase noise and other indicators	Ref.
Fundamental single-loop OEO	Pure microwave signal	First proposed	Fixed	-110 dBc/Hz @ 10 kHz	[8]
Multi-loop OEO		Phase noise and SMSR improvement		-140 dBc/Hz @ 10 kHz SMSR > 70 dB	[10]
Dual-loop and dual-modulation		SMSR improvement		-104 dBc/Hz @ 10 kHz SMSR >70 dB	[12]
Dual-loop OEO based on PolM and PS-FBG		Tunable frequency and phase	6.6-13.1 GHz	-101.9 dBc/Hz @ 10 kHz	[14]
Single-loop OEO based on F-P etalon		Low phase noise	Discrete tunability	-100 dBc/Hz @ 10 kHz	[18]
Single-loop OEO based on PM and PS-FBG		Wideband frequency tunability	3-28 GHz	-102 dBc/Hz @ 10 kHz	[20]
Single-loop OEO based on PM and SBS effect			7-40 GHz	-128 dBc/Hz @ 10 kHz	[22]
Integrated OEO		Highly integrated	Within 20MHz	−92 dBc/Hz @ 1 MHz	[24]
Injection locking OEO employing two EBPFs	Coherent dual-frequency signal	Dual-frequency with low phase noise	Fixed	-141 dBc/Hz @ 10 kHz	[29]
OEO based on dual-band MPF	Frequency-hopping signal	High-speed and wideband	8.65-17.1 GHz	TBWP=700	[30]
Fourier domain mode-locked OEO	Linearly chirped microwave waveform	Breaking the limitation of mode building time	CF: 5-17 GHz BW: 0.8-7.5 GHz	TBWP=166650	[33]
Frequency-scanning OEO	Linearly & non-linearly chirped microwave waveform, frequency-hopping signal and phase-coded signal.	Arbitrary microwave waveform generation	Around 7 GHz	-108 dBc/Hz @ 10 kHz	[41]
OEO based on dual-band EBPF	Frequency-hopping signal	Dissipative microwave photonic solitons generation	Fixed	−133.1 dBc/Hz @ 10 kHz	[44]
Broadband OEO	Optoelectronic chaos	Broadband chaos generation	Below 8GHz	Lyapunov exponent of ~ 0.03 ns^{-1}	[46]
Period-doubling OEPO	Coherent dual-frequency signal and frequency-hopping signal	Multi-format microwave generation	6.5-12 GHz	-121.5 dBc/Hz @ 10 kHz	This work

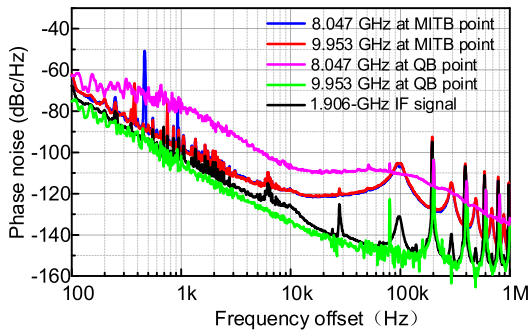

Fig. 12. Phase noise performance of the output dual-frequency signals at different bias points and the intermediate-frequency (IF) signal generated by frequency mixing.

injected signal become the optical carrier in the OEPO loop, so its phase noise performance is collectively limited by that of the injected signal (black line) and the oscillation system. It should be noted that phase noise performance at low frequency offsets (1–5 kHz) does improve with increased fiber length.

To verify the inherent phase coherence of the dual-frequency signal, the two frequency components are separated by band-pass filters and then combined using an electrical mixer. The phase noise curves for the output intermediate-frequency (IF) signal (black line) and the original frequency components (red and blue lines) are shown in Fig. 12. Compared to the frequency components of the dual-frequency signal, the phase noise performance of the intermediate-frequency signal shows considerable improvement, indicating that the two frequency components of the dual-frequency signal are phase coherent. It is worth noting that to achieve a phase-coherent dual-frequency signal, the MZM must be biased at the MITB point. Although the OEPO can generate a dual-frequency signal when the MZM is set at the quadrature bias (QB) point, the signal is not phase coherent. The phase noise curves for the MZM biased at the QB point are also shown in Fig. 12. The phase noise curves for the 8.047-GHz (pink line) and 9.953-GHz (green line) frequency components show a significant difference. The phase noise of the 9.953 GHz component is similar to that of a free-running OEO, while the phase noise of the 8.047 GHz component resembles that of the injected signal. This discrepancy occurs because the OEPO behaves as a frequency-mixing system rather than a parametric oscillation system when the MZM is set to the QB point.

C. Hopf Bifurcation

To investigate how the amplitudes of the oscillating signal vary, different loop gains are achieved in the OEPO system by separately adjusting the insertion loss of the VOA and the injected power of the RF source. Fig. 13(a) shows how the amplitudes of the two frequency components change with the optical carrier power, while the injected power is fixed at 18 dBm. The amplitudes exhibit Hopf bifurcations at an optical power (input power to the MZM) of approximately 10.5 dBm. Fig. 13(b)

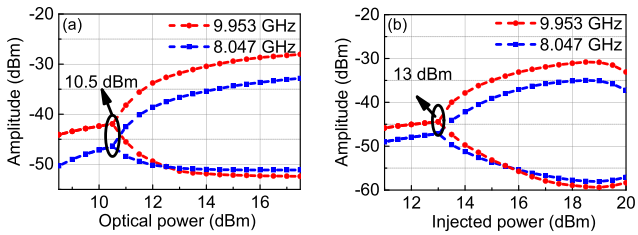

Fig. 13. (a) Measured amplitudes varying with the power of optical carrier. (b) Measured amplitudes varying with the injected power of microwave source.

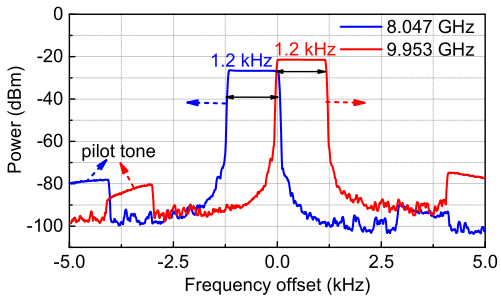

Fig. 14. Frequency drifts of the two frequency components over 10 minutes at max-hold mode (RBW = 100 Hz).

illustrates how the amplitudes vary with the injected power, while the optical power is fixed at 14 dBm. The amplitudes exhibit Hopf bifurcations at an injected power of approximately 13 dBm and reach maximum values at about 19 dBm. Additionally, the experimental results for amplitude variations near the bifurcation point are consistent with the simulation results presented in Fig. 3.

D. Long-Term Stability

To assess the frequency stability of the proposed OEPO, the frequency drift of the output dual-frequency signal is evaluated using a PNA in max-hold mode. As shown in Fig. 14, the frequency span and RBW are set to 10 kHz and 100 Hz, respectively. Over a period of 10 minutes, the measured frequency drifts of both frequency components remain within 1.2 kHz, indicating good stability performance. Notably, no mode hopping is observed during the measurement. The frequency drifts are mainly induced by the loop delay variation caused by slow temperature changes of the long single-mode fiber. This issue could be mitigated with temperature control [61] or dynamic feedback compensation [62]. Interestingly, the frequency drift directions of the two frequency components are opposite, which satisfy the complementary characteristic of the two frequency components. To prevent bias drift of the MZM during long-term measurement, a bias point controller with a 4-kHz pilot tone is employed, resulting in frequency offset peaks of ± 4 kHz on both sides of the carrier frequencies.

IV. Conclusion

In this paper, a period-doubling OEPO for reconfigurable and tunable microwave waveform generation is proposed and experimentally demonstrated. Different from conventional OEO, the oscillating period in this system is twice the loop delay of the OEPO. By adjusting the loop gain, both dual-frequency and frequency-hopping microwave signals can be generated. A comparison of some previous OEOs for microwave generation and this work is listed in Table I. To our knowledge, this is the first report for the microwave generation of both coherent dual-frequency signal and frequency-hopping signal with large frequency tunability. The frequency tuning range in this experiment spans from 6.5 to 12 GHz, limited by the bandwidth of the broadband filter. The phase noise of the dual-frequency signal is approximately -121.5 dBc/Hz at a 10 kHz offset, lower than that of both the injection signal and the free-running OEO. Additionally, the phase noise performance of the frequency-hopping signal shows significant improvement compared to commercial frequency-hopping sources. This OEPO, utilizing a period-doubling oscillation mechanism and providing reconfigurable microwave waveform capabilities, has potential applications in emerging wireless communications and advanced electronic warfare systems.

References

[1] D. Tse and P. Viswanath, *Fundamentals of Wireless Communication*. Cambridge, U.K.: Cambridge Univ. Press, 2005.
[2] M. I. Skolnik, *Radar Handbook*, 3rd ed. New York, NY, USA: McGraw-Hill, 2008.
[3] A. E. Spezio, "Electronic warfare systems," *IEEE Trans. Microw. Theory Technol.*, vol. 50, no. 3, pp. 633–644, Mar. 2002.
[4] S. Pan and Y. Zhang, "Microwave photonic radars," *J. Lightw. Technol.*, vol. 38, no. 19, pp. 5450–5484, Oct. 2020.
[5] S. Pan, X. Ye, Y. Zhang, and F. Zhang, "Microwave photonic array radars," *IEEE J. Microw.*, vol. 1, no. 1, pp. 176–190, Jan. 2021.
[6] F. Herzel, M. Pierschel, P. Weger, and M. Tiebout, "Phase noise in a differential CMOS voltage-controlled oscillator for RF applications," *IEEE Trans. Circuits Syst. II: Analog Digit. Signal Process.*, vol. 47, no. 1, pp. 11–15, Jan. 2000.
[7] C. S. Lam, "A review of the recent development of MEMS and crystal oscillators and their impacts on the frequency control products industry," in *Proc. 2008 IEEE Ultrasonics Symp.*, Beijing, China, 2008, pp. 694–704.
[8] X. S. Yao and L. Maleki, "Optoelectronic microwave oscillator," *J. Opt. Soc. Am. B*, vol. 13, no. 8, pp. 1725–1735, Aug. 1996.
[9] X. S. Yao and L. Maleki, "Optoelectronic oscillator for photonic systems," *IEEE J. Quantum Electron.*, vol. 32, no. 7, pp. 1141–1149, Jul. 1996.
[10] X. S. Yao and L. Maleki, "Multiloop optoelectronic oscillator," *IEEE J. Quantum Electron.*, vol. 36, no. 1, pp. 79–84, Jan. 2000.
[11] L. Maleki, "The optoelectronic oscillator," *Nat. Photon.*, vol. 5, no. 12, pp. 728–730, Dec. 2011.
[12] J.-Y. Kim, J.-H. Jo, W.-Y. Choi, and H.-K. Sung, "Dual-loop dual-modulation optoelectronic oscillators with highly suppressed spurious tones," *IEEE Photon. Technol. Lett.*, vol. 24, no. 8, pp. 706–708, Apr. 2012.
[13] D. Eliyahu and L. Maleki, "Low phase noise and spurious level in multi-loop opto-electronic oscillators," in *Proc. IEEE Int. Freq. Control Symp. PDA Exhib. Jointly 17th Eur. Freq. Time Forum*, Tampa, FL, USA, 2003, pp. 405–410.
[14] L. Gao, M. Wang, X. Chen, and J. Yao, "Frequency- and phase-tunable optoelectronic oscillator," *IEEE Photon. Technol. Lett.*, vol. 25, no. 11, pp. 1011–1013, Jun. 2013.
[15] G. Zhang et al., "Hybrid-integrated wideband tunable optoelectronic oscillator," *Opt. Exp.*, vol. 31, no. 10, pp. 16929–16938, May 2023.
[16] X. Zhang et al., "Simple frequency-tunable optoelectronic oscillator using integrated multi-section distributed feedback semiconductor laser," *Opt. Exp.*, vol. 27, no. 5, pp. 7036–7046, Mar. 2019.

[17] A. Coillet, R. Henriet, P. Salzenstein, K. P. Huy, L. Larger, and Y. K. Chembo, "Time-domain dynamics and stability analysis of optoelectronic oscillators based on whispering-gallery mode resonators," *IEEE J. Sel. Top. Quantum Electron.*, vol. 19, no. 5, Sep./Oct. 2013, Art. no. 6000112.

[18] I. Ozdur, D. Mandridis, N. Hoghooghi, and P. J. Delfyett, "Low noise optically tunable opto-electronic oscillator with Fabry–Perot etalon," *J. Lightw. Technol.*, vol. 28, no. 21, pp. 3100–3106, Nov. 2010.

[19] X. Xie et al., "Wideband tunable optoelectronic oscillator based on a phase modulator and a tunable optical filter," *Opt. Lett.*, vol. 38, no. 5, pp. 655–657, Mar. 2013.

[20] W. Li and J. Yao, "A wideband frequency tunable optoelectronic oscillator incorporating a tunable microwave photonic filter based on phase-modulation to intensity-modulation conversion using a phase-shifted fiber bragg grating," *IEEE Trans. Microw. Theory Techn.*, vol. 60, no. 6, pp. 1735–1742, Jun. 2012.

[21] Z. Tang et al., "Tunable optoelectronic oscillator based on a polarization modulator and a chirped FBG," *IEEE Photon. Technol. Lett.*, vol. 24, no. 17, pp. 1487–1489, Sep. 2012.

[22] H. Peng et al., "Wideband tunable optoelectronic oscillator based on the deamplification of stimulated brillouin scattering," *Opt. Exp.*, vol. 25, no. 9, pp. 10287–10305, May 2017.

[23] H. Tang, Y. Yu, Z. Wang, L. Xu, and X. Zhang, "Wideband tunable optoelectronic oscillator based on a microwave photonic filter with an ultra-narrow passband," *Opt. Lett.*, vol. 43, no. 10, pp. 2328–2331, May 2018.

[24] J. Tang et al., "Integrated optoelectronic oscillator," *Opt. Exp.*, vol. 26, no. 9, pp. 12257–12265, Apr. 2018.

[25] W. Zhang and J. Yao, "Silicon photonic integrated optoelectronic oscillator for frequency-tunable microwave generation," *J. Lightw. Technol.*, vol. 36, no. 19, pp. 4655–4663, Oct. 2018.

[26] M. F. Lewis, "Novel RF oscillator using optical components," *Electron. Lett.*, vol. 28, Jan. 1992, Art. no. 31.

[27] H. Peng, P. Lei, X. Xie, and Z. Chen, "Photonic RF synthesizer based on a phase-locked optoelectronic oscillator using anti-stokes loss spectrum of stimulated Brillouin scattering," *IEEE Photon. J.*, vol. 14, no. 3, Jun. 2022, Art. no. 5531508.

[28] B. Gao, F. Zhang, P. Zhou, and S. Pan, "A frequency-tunable two-tone RF signal generator by polarization multiplexed optoelectronic oscillator," *IEEE Microw. Wireless Compon. Lett.*, vol. 27, no. 2, pp. 192–194, Feb. 2017.

[29] S. Liu, C. Du, L. Yang, M. Liu, Z. Tang, and S. Pan, "Coherent dual-frequency signal generation in an optoelectronic oscillator," *Opt. Lett.*, vol. 48, no. 11, pp. 2921–2924, Jun. 2023.

[30] W. Li, Z. Weifeng, and J. Yao, "Frequency-hopping microwave waveform generation based on a frequency-tunable optoelectronic oscillator," in *Proc. IEEE OFC 2014*, San Francisco, CA, USA, 2014, pp. 1–3.

[31] W. Li, F. Kong, and J. Yao, "Stable and frequency-hopping-free microwave generation based on a mutually injection-locked optoelectronic oscillator and a dual-wavelength single-longitudinal-mode fiber laser," *J. Lightw. Technol.*, vol. 32, no. 21, pp. 4174–4179, Nov. 2014.

[32] Z. Weinan et al., "High-speed frequency-hopping signal generator with a stimulated Brillouin scattering-based optoelectronic oscillator," *Opt. Eng.*, vol. 59, no. 2, Feb. 2020, Art. no. 027101.

[33] T. Hao et al., "Breaking the limitation of mode building time in an optoelectronic oscillator," *Nat. Commun.*, vol. 9, no. 1, May 2018, Art. no. 1839.

[34] T. Hao, J. Tang, W. Li, N. Zhu, and M. Li, "Tunable Fourier domain mode-locked optoelectronic oscillator using stimulated Brillouin scattering," *IEEE Photon. Technol. Lett.*, vol. 30, no. 21, pp. 1842–1845, Nov. 2018.

[35] T. Hao, J. Tang, W. Li, N. Zhu, and M. Li, "Fourier domain mode locked optoelectronic oscillator based on the deamplification of stimulated Brillouin scattering," *OSA Continuum*, vol. 1, no. 2, pp. 408–415, Oct. 2018.

[36] T. Hao, J. Tang, W. Li, N. Zhu, and M. Li, "Harmonically Fourier domain mode-locked optoelectronic oscillator," *IEEE Photon. Technol. Lett.*, vol. 31, no. 6, pp. 427–430, Mar. 2019.

[37] T. Hao, J. Tang, N. Shi, W. Li, N. Zhu, and M. Li, "Dual-chirp Fourier domain mode-locked optoelectronic oscillator," *Opt. Lett.*, vol. 44, no. 8, pp. 1912–1915, Apr. 2019.

[38] Z. Zeng et al., "Frequency-definable linearly chirped microwave waveform generation by a Fourier domain mode locking optoelectronic oscillator based on stimulated Brillouin scattering," *Opt. Exp.*, vol. 28, no. 9, pp. 13861–13870, Apr. 2020.

[39] L. Zhang et al., "Frequency-sweep-range-reconfigurable complementary linearly chirped microwave waveform pair generation by using a Fourier domain mode locking optoelectronic oscillator based on stimulated Brillouin scattering," *IEEE Photon. J.*, vol. 12, no. 3, Jun. 2020, Art. no. 5501010.

[40] Y. Chen, S. Liu, and S. Pan, "Multi-format signal generation using a frequency-tunable optoelectronic oscillator," *Opt. Exp.*, vol. 26, no. 3, pp. 3404–3420, Feb. 2018.

[41] Y. Chen, P. Zuo, and T. Shi, "Optoelectronic oscillator for arbitrary microwave waveform generation," *J. Lightw. Technol.*, vol. 39, no. 19, pp. 6033–6044, Oct. 2021.

[42] W. Li, F. Kong, and J. Yao, "Arbitrary microwave waveform generation based on a tunable optoelectronic oscillator," *J. Lightw. Technol.*, vol. 31, no. 23, pp. 3780–3786, Dec. 2013.

[43] W. Weng, J. He, A. Kaszubowska-Anandarajah, P. M. Anandarajah, and T. J. Kippenberg, "Microresonator dissipative Kerr solitons synchronized to an optoelectronic oscillator," *Phys. Rev. A*, vol. 17, no. 2, Feb. 2022, Art. no. 024030.

[44] T. Hao, H. Ding, W. Li, N. Zhu, Y. Dai, and M. Li, "Dissipative microwave photonic solitons in spontaneous frequency-hopping optoelectronic oscillators," *Photon. Res.*, vol. 10, no. 5, pp. 1280–1289, May 2022.

[45] Y. K. Chembo, A. Hmima, P.-A. Lacourt, L. Larger, and J. M. Dudley, "Generation of ultralow jitter optical pulses using optoelectronic oscillators with time-lens soliton-assisted compression," *J. Lightw. Technol.*, vol. 27, no. 22, pp. 5160–5167, Nov. 2009.

[46] K. E. Callan, L. Illing, Z. Gao, D. J. Gauthier, and E. Schöll, "Broadband chaos generated by an optoelectronic oscillator," *Phys. Rev. Lett.*, vol. 104, no. 11, Mar. 2010, Art. no. 113901.

[47] L. Larger and J. M. Dudley, "Optoelectronic chaos," *Nature*, vol. 465, no. 7294, pp. 41–42, May 2010.

[48] B. Romeira, F. Kong, W. Li, J. M. L. Figueiredo, J. Javaloyes, and J. Yao, "Broadband chaotic signals and breather oscillations in an optoelectronic oscillator incorporating a microwave photonic filter," *J. Lightw. Technol.*, vol. 32, no. 20, pp. 3933–3942, Oct. 2014.

[49] P. Mu, W. Pan, S. Xiang, N. Li, X. Liu, and X. Zou, "Fast physical and pseudo random number generation based on a nonlinear optoelectronic oscillator," *Mod. Phys. Lett. B*, vol. 29, no. 24, Sep. 2015, Art. no. 1550142.

[50] Y. K. Chembo, L. Larger, and P. Colet, "Nonlinear dynamics and spectral stability of optoelectronic microwave oscillators," *IEEE J. Quantum Electron.*, vol. 44, no. 9, pp. 858–866, Sep. 2008.

[51] B. Romeira, J. M. L. Figueiredo, C. N. Ironside, K. Seunarine, and J. Javaloyes, "Nonlinear dynamics of a Liénard delayed-feedback optoelectronic oscillator," in *Proc. INDS'11 ISTET'11*, Klagenfurt am Wörthersee, Austria, 2011, pp. 1–5.

[52] K. Xu et al., "Long-term stability improvement of tunable optoelectronic oscillator using dynamic feedback compensation," *Opt. Exp.*, vol. 23, no. 10, pp. 12935–12941, May 2015.

[53] Y. K. Chembo, D. Brunner, M. Jacquot, and L. Larger, "Optoelectronic oscillators with time-delayed feedback," *Rev. Mod. Phys.*, vol. 91, no. 3, Sep. 2019, Art. no. 035006.

[54] X. Zhang, Z. Li, B. Li, R. Wu, and W. Hong, "Nonlinear dynamics of the dual-loop optoelectronic oscillator based on polarization multiplexing," *Chaos, Soliton Fract.*, vol. 174, Sep. 2023, Art. no. 113938.

[55] T. Hao et al., "Optoelectronic parametric oscillator," *Light-Sci. Appl.*, vol. 9, no. 1, Jun. 2020, Art. no. 102.

[56] S. Liu, K. Lv, J. Fu, L. Wu, W. Pan, and S. Pan, "Wideband microwave frequency division based on an optoelectronic oscillator," *IEEE Photon. Technol. Lett.*, vol. 31, no. 5, pp. 389–392, Mar. 2019.

[57] L. Larger, P.-A. Lacourt, S. Poinsot, and M. Hanna, "From flow to map in an experimental high-dimensional electro-optic nonlinear delay oscillator," *Phys. Rev. Lett.*, vol. 95, no. 4, Jul. 2005, Art. no. 043903.

[58] Y. K. Chembo, L. Larger, and P. Colet, "Nonlinear dynamics and spectral stability of optoelectronic microwave oscillators," *IEEE J. Quantum Electron.*, vol. 44, no. 9, pp. 858–866, Sep. 2008.

[59] Y. Kouomou Chembo, L. Larger, H. Tavernier, R. Bendoula, E. Rubiola, and P. Colet, "Dynamic instabilities of microwaves generated with optoelectronic oscillators," *Opt. Lett.*, vol. 32, no. 17, pp. 2571–2573, Sep. 2007.

[60] M. Ha and Y. K. Chembo, "Nonlinear dynamics of continuously tunable optoelectronic oscillators based on stimulated Brillouin amplification," *Opt. Exp.*, vol. 29, no. 10, pp. 14630–14648, May 2021.

[61] D. Eliyahu, K. Sariri, M. Kamran, and M. Tokhmakhian, "Improving short and long term frequency stability of the opto-electronic oscillator," in *Proc. 2002 IEEE Int. Freq. Control Symp. PDA Exhib.*, New Orleans, LA, USA, May 2002, pp. 580–583.

[62] K. Xu et al., "Long-term stability improvement of tunable optoelectronic oscillator using dynamic feedback compensation," *Opt. Exp.*, vol. 23, no. 10, pp. 12935–12941, May 2015.